ADVANCED FUNCTIONAL MATERIALS
www.afm-journal.de

High-Voltage Aqueous Mg-Ion Batteries Enabled by Solvation Structure Reorganization

Qiang Fu, Xiaoyu Wu, Xianlin Luo, Sylvio Indris, Angelina Sarapulova, Marina Bauer, Zhengqi Wang, Michael Knapp, Helmut Ehrenberg, Yingjin Wei,* and Sonia Dsoke*

Herein, an eco-friendly and high safety aqueous Mg-ion electrolyte (AME) with a wide electrochemical stability window (ESW) ≈3.7 V, containing polyethylene glycol (PEG) and low-concentration salt (0.8 m $Mg(TFSI)_2$), is proposed by solvation structure reorganization of AME. The PEG agent significantly alters the Mg^{2+} solvation and hydrogen bonds network of AMEs and forms the direct coordination of Mg^{2+} and $TFSI^-$, thus enhancing the physicochemical and electrochemical properties of electrolytes. As an exemplary material, V_2O_5 nanowires are tested in this new AME and exhibit initial high discharge/charge capacity of 359/326 mAh g^{-1} and high capacity retention of 80% after 100 cycles. The high crystalline α-V_2O_5 shows two 2-phase transition processes with the formation of ε-$Mg_{0.6}V_2O_5$ and Mg-rich $Mg_xV_2O_5$ (x ≈1.0) during the first discharge. Mg-rich $Mg_xV_2O_5$ (x ≈1.0) phase formed through electrochemical Mg-ion intercalation at room temperature is for the first time observed via XRD. Meanwhile, the cathode electrolyte interphase (CEI) in aqueous Mg-ion batteries is revealed for the first time. MgF_2 originating from the decomposition of $TFSI^-$ is identified as the dominant component. This work offers a new approach for designing high-safety, low-cost, eco-friendly, and large ESW electrolytes for practical and novel aqueous multivalent batteries.

1. Introduction

Aqueous magnesium-ion batteries (AMIBs) have become very attractive recently due to the low cost, high safety, high conductivity of aqueous electrolytes, and rich resources of Mg.[1] Generally, the specific energy of AMIBs largely depends on the capacity and working potential of the cathode material. Among numerous cathode materials under investigation, vanadium pentoxide (V_2O_5) has been considered as a promising one owing to its large theoretical capacity (294 mAh g^{-1} when considering 1 mol of Mg^{2+} per mol V_2O_5) and high average working voltage of ≈2.4 V,[2] which results in a large specific energy (> 600 Wh kg^{-1}). Practically, in contrast to theoretical predictions, the V_2O_5 nanoclusters/carbon composites show an initial discharge capacity of 300 mAh g^{-1} in the voltage range of 0.5–2.8 V versus Mg^{2+}/Mg.[2i] Despite this, the cycle stability of this kind of high voltage cathode material has been seriously limited by the low electrochemical stability window (ESW, 1.3–2 V) of aqueous Mg-ion electrolyte (AME).[1b,3] The ESW of aqueous electrolytes strongly depends on the salts and solvents, electrolyte-electrode interphases, and electrolyte additives.[4] Suo et al.[4a] proposed water-in-salt electrolytes (WiSE) to expand the ESW of aqueous Li-ion electrolytes to ≈3.0 V using 21 m ("m" means "mol/kg") lithium bis(trifluoromethanesulfonyl) imide (LiTFSI). The hydrate molten salt Li-ion electrolytes were reported to show a very high ESW (3.8[4c] and 5 V[4d]). Researchers also made great progress in AMIBs. For instance, Wang et al.[1b] expanded the ESW of AME from 1.3 to 2.0 V using 4 m magnesium bis(trifluoromethanesulfonyl)imide ($Mg(TFSI)_2$) and enabled the use of high-voltage cathode $Mg_xLiV_2(PO_4)_3$. Irrespectively, concentrated WiSEs still have several serious drawbacks such as high viscosity, low ionic conductivity, high desolvation energy, and high cost, which impede their practical applications.[5]

Molecular crowding is a common feature in living cells where water activity is substantially suppressed by molecular crowding agents[6] via altering hydrogen-bonding structure.[7] Hence, it makes sense to tune electrolyte solvation structure using a water-miscible solvent to decrease water activity, thereby achieving high-voltage aqueous electrolytes with a low-concentration salt. This idea has been demonstrated for aqueous Li-ion electrolytes recently where a molecular crowding agent polyethylene glycol 400 (PEG 400) was added into LiTFSI-H_2O, which

Q. Fu, X. Luo, S. Indris, A. Sarapulova, M. Bauer, Z. Wang, M. Knapp, H. Ehrenberg, S. Dsoke
Institute for Applied Materials (IAM)
Karlsruhe Institute of Technology (KIT)
Hermann-von-Helmholtz-Platz 1,
D-76344, Eggenstein-Leopoldshafen, Germany
E-mail: qiang.fu@kit.edu

X. Wu, Y. Wei
Key Laboratory of Physics and Technology for Advanced Batteries (Ministry of Education)
College of Physics
Jilin University
2699 Qianjin Street, Changchun 130012, P. R. China
E-mail: yjwei@jlu.edu.cn

H. Ehrenberg, S. Dsoke
Helmholtz Institute Ulm for Electrochemical Energy Storage (HIU)
Helmholtzstrasse 11, 89081 Ulm, Germany

The ORCID identification number(s) for the author(s) of this article can be found under https://doi.org/10.1002/adfm.202110674.

DOI: 10.1002/adfm.202110674

had an expanded ESW of 3.2 V and therefore enabled high-efficient working of a $LiMn_2O_4/Li_4Ti_5O_{12}$ full cell over 300 cycles.[8] Inspired by this work, herein, we propose an eco-friendly and high-safety AME using the PEG and low-salt concentration $Mg(TFSI)_2$ salt. The optimized 0.8 m $Mg(TFSI)_2$-85%PEG-15%H_2O electrolyte owns a wide ESW of ≈3.7 V. Hence, it enables the usage of high-voltage V_2O_5 cathode material, which exhibits a large initial discharge capacity of 359 mAh g^{-1} and ≈80% capacity retention after 100 cycles. Using this high efficient AMIB system, the electrochemical reaction mechanism of V_2O_5 in AMIBs is intensively studied by synchrotron and lab based X-ray spectroscopies. V_2O_5 experiences two steps of structural transitions during Mg^{2+} intercalation. Accompanied with Mg^{2+} intercalation, a cathode electrolyte interface (CEI) film forms on the surface of the V_2O_5 electrode and then decomposes during the following de-intercalation process. This work not only provides an indepth experimental and theoretical approach for designing high-safety, low-cost, and high-voltage AMEs and high-performance cathodes for AMIBs but also offers a deep understanding on the reaction mechanism of vanadium oxide cathode material in AMIBs.

2. Results and Discussion

2.1. Solvation Structure Reorganization of Aqueous Mg-Ion Electrolytes (AMEs)

PEG 400 is considered an ideal crowding agent for AMEs due to its unique advantages such as miscibility with water, inertness, low toxicity, and low cost. To study the properties of AMEs, a series of 0.8 m $Mg(TFSI)_2$-xPEG-(1-x)H_2O (x = 0%, 75%, 80%, 85%, 90%, and 95%) were prepared. With the addition of PEG, the viscosity of the electrolytes strongly increases and the ionic conductivity notably decreases (Figure S1 and Table S1, Supporting Information), which well matches with the Walden's rule.[9] The ionic conductivity of the electrolytes with 75–85%PEG is close to that of Li-ion WiSEs and liquid Mg-ion electrolytes and much higher than that of solid/gel Mg-ion electrolytes (Table S2, Supporting Information). The ESWs of the electrolytes are determined by linear sweep voltammetry (LSV) using glassy carbon (GC) as a working electrode. Compared to PEG-free 0.8 m $Mg(TFSI)_2$-100%H_2O, the ESW of the AME expands with increasing the amount of PEG, where both the O_2 and H_2 evolution potentials are pushed beyond the thermodynamic stability of water (**Figure 1**a). The electrolyte with 95%PEG (Figure 1b) shows an onset of reduction at 1.07 V versus Mg^{2+}/Mg and then reaches a plateau at 0.48 V versus Mg^{2+}/Mg. Different from the other electrolytes, the absence of H_2 evolution could be due to the lack of "free" water in this electrolyte. It seems $TFSI^-$ reduction for the electrolytes with 80–95%PEG results in a passivation process, similar to the 21m-LiTFSI WiSE reported by Suo et al.[4a] Consequently, the plateau current reduces from 11.9 (80%PEG) to 4.9 (85%PEG), 3.7 (90%PEG), and 3.5 μA cm^{-2} (95%PEG). This passivation, in turn, suppresses H_2 evolution. O_2 evolution at the cathode side is also suppressed by the presence of PEG, but a clear passivation process is not observed (Figure 1c). Overall, an ESW of ≈3.7 V is obtained for 0.8 m $Mg(TFSI)_2$-85%PEG-15%H_2O, which is 2.3 times as wide as that of ≈1.6 V for the PEG-free electrolyte.

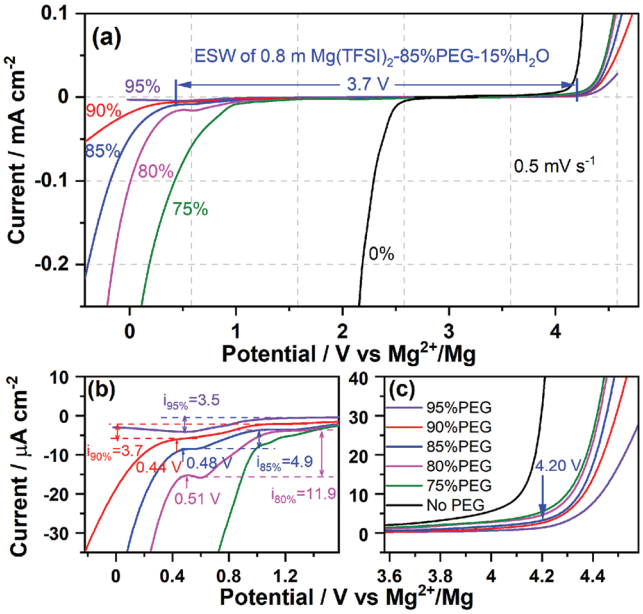

Figure 1. The linear sweep voltammetry (LSV) of 0.8 m $Mg(TFSI)_2$-xPEG-(1-x)H_2O (x = 0%, 75%, 80%, 85%, 90%, and 95%) on glassy carbon (GC) between −3.0 and 2.2 V versus AgCl/Ag at 0.5 mV s^{-1}, where potentials have been converted to Mg^{2+}/Mg reference for convenience based on the voltage difference of 2.58 V between AgCl/Ag and Mg^{2+}/Mg. a) The overall ESW and enlarged regions of [−0.22 V, 1.58 V] and [3.58 V, 4.58 V] versus Mg^{2+}/Mg in both b) anodic and c) cathodic sides.

This ESW is the widest value up-to-date reported for AMEs and also much wider than most representative non-aqueous Mg-ion electrolytes (Table S3, Supporting Information), highlighting the great potential of 0.8 m $Mg(TFSI)_2$-85%PEG-15%H_2O as a high voltage Mg-ion electrolyte. Moreover, the use of low-salt concentration and low-cost solvent significantly reduces the cost of AMIBs.

Flammability test shows that this electrolyte is non-flammable demonstrating its superior safety properties (Figure S2 and Videos S1–S4, Supporting Information). Furthermore, LSV test of 0.8 m $Mg(TFSI)_2$-85%PEG-15%H_2O was also performed on stainless steel foil (SS) since SS is a common current collector. The electrolyte shows on SS an overall ESW of ≈2.3 V (Figure S3, Supporting Information). Besides, a plateau-like curve is seen at ≈4.2 V versus Mg^{2+}/Mg due to the passivation process related to the oxidation of $TFSI^-$.

Nuclear magnetic resonance (NMR) and Fourier-transform infrared spectroscopy (FTIR) were carried out to reveal how the PEG crowding agent impacts the physicochemical properties of the AMEs. ^1H spectrum of 0.8 m $Mg(TFSI)_2$-100%H_2O exhibits a chemical shift at 4.84 ppm (**Figure 2**a), corresponding to H_2O solvent.[10] Upon adding PEG from 75% to 85%, the ^1H peak of H_2O weakens and shifts to higher values, indicating the decrease of electron density around H atoms and the shortening of H–O bond in H_2O. Meanwhile, one ^1H peak of PEG can be observed at 3.74 ppm and initially does not show any shift in the range of 75–85%PEG, showing a slightly higher value compared with pure PEG solvent (3.70 ppm). By further adding PEG (90–95%), the ^1H peak of H_2O disappears and the one of PEG shows strong broadening and becomes almost invisible due to the high viscosity and disordered environment. The trend of the

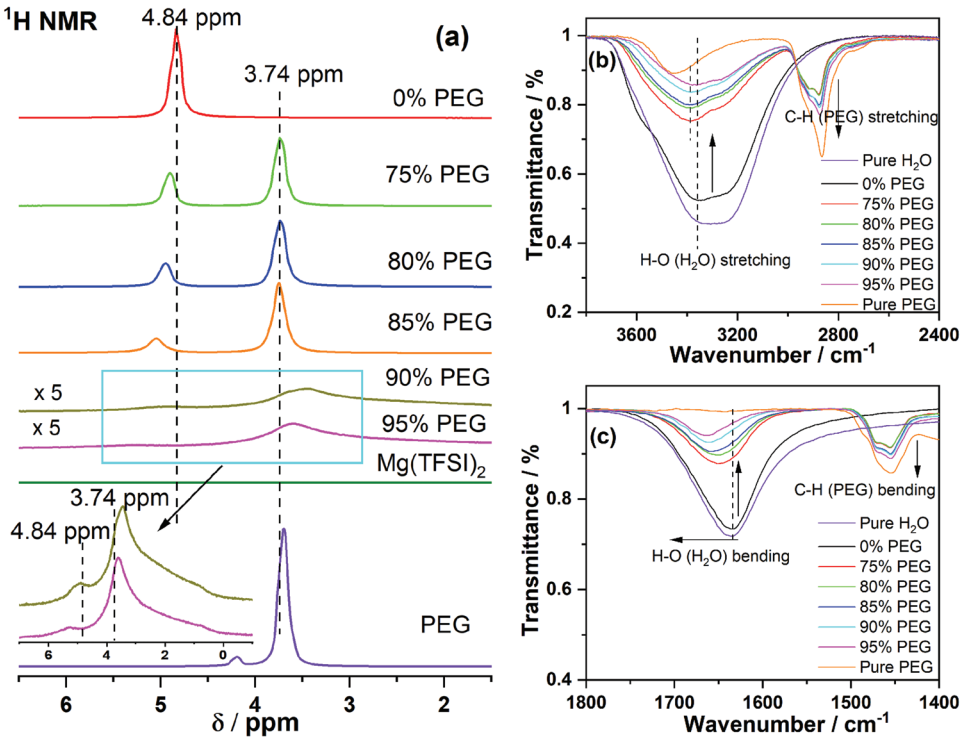

Figure 2. a) ^{1}H NMR and b,c) FTIR spectra of 0.8 m $Mg(TFSI)_2$-xPEG-(1-x)H_2O (x = 0%, 75%, 80%, 85%, 90%, and 95%) and their comparison with pure $Mg(TFSI)_2$ and PEG. PEG solvent reference shows ^{1}H chemical shift at 4.20 ppm (OH-) and 3.70 ppm (CH_2) and $Mg(TFSI)_2$ has no ^{1}H chemical shift.

^{1}H NMR peak of H_2O shifting to higher values for increasing PEG content is different from ^{1}H NMR observations on LiTFSI-PEG-H_2O[8] and LiTFSI-based WiSE[11] both of which show shifts to lower values due to the different environment of hydrogen in these electrolytes. This may be attributed to the interactions of Mg^{2+}, $TFSI^-$, and PEG with H_2O, each of which could influence the solvent structures especially coordination and hydrogen bonds (HBs). To prove this, molecular dynamics (MD) calculations were performed to study the HBs of different electrolytes (Table S4, Supporting Information). The HBs of 0.8 m $Mg(TFSI)_2$-100%H_2O are contributed by $TFSI^-$-H_2O interaction (≈5.4 per $TFSI^-$) and H_2O-H_2O interaction (≈1.5 per H_2O). While 0.8 m $Mg(TFSI)_2$-85%PEG-15%H_2O shows an additional interaction of PEG-H_2O (≈1.9 per PEG) and the contributions from $TFSI^-$-H_2O and H_2O-H_2O are reduced to ≈1.6 (per $TFSI^-$) and ≈1 (per H_2O), respectively. The changes of HBs, therefore, affect the ^{1}H chemical shift of the electrolytes, as observed in the NMR experiments. Besides, the lifetime of HBs increases from 50.86 ps (0.8 m $Mg(TFSI)_2$-100%H_2O) to 79.33 ps (0.8 m $Mg(TFSI)_2$-85%PEG-15%H_2O), which demonstrates that the PEG crowding agent improves the stability of the AMEs.

Figure 2b,c shows the FTIR spectra of different electrolytes. The FTIR spectrum of H_2O is dominated by two broad peaks at 3297 and 1636 cm^{-1}, which are attributed to the stretching and bending vibrations of H–O bond, respectively. PEG shows three FTIR peaks at 3451, 2864, and 1454 cm^{-1}, corresponding to H-O stretching, C–H stretching, and C–H bending, respectively. Upon adding PEG, the C–H stretching and bending peaks of PEG exhibit intensities decrease but their peak positions remain unchanged, demonstrating the structural stability of PEG. In contrast, the H–O stretching and bending peaks of H_2O shift to 3399 and 1658 cm^{-1} with the increase of PEG to 85%, accompanied by intensities reduction. This significant blueshift demonstrates the strengthening of the H-O bond, which could be ascribed to the interaction between PEG and H_2O (PEG-H_2O) and the reorganization of the proton donor framework, as well as the coordination of Mg^{2+}, H_2O, and PEG. Due to the inductive effect of the alkyl groups in PEG,[12] the O atom in PEG has a higher negative charge density than that in H_2O, which promotes the H atom in H_2O to donate electrons and therefore forms HBs between H_2O and PEG. Consequently, the PEG crowding agent strengthens the H–O bond of the AME. Overall, a higher potential is required to break the H–O bond (water decomposition), expanding the ESW of the electrolytes.

Furthermore, density functional theory (DFT) and MD calculations were conducted to monitor the structure changes and dissolution mechanism of electrolytes at the atomic level. The simulated geometrical structures of 0.8 m $Mg(TFSI)_2$-100%H_2O and 0.8 m $Mg(TFSI)_2$-85%PEG-15%H_2O are shown in **Figure 3**a,b. Total energy calculations and root-mean-square deviation (RMSD) of Mg^{2+} confirm that both electrolyte systems are stabilized at equilibrium states (Figure S4, Supporting Information). To quantitatively analyze the solvation structure, short-range correlations of the electrolytes including radial distribution function (RDF) and corresponding integrated coordination numbers (ICN) are presented (Figure 3c,d and Table S5: Supporting Information). The g(r) profiles of Mg^{2+}-H_2O in 0.8 m $Mg(TFSI)_2$-100%H_2O and 0.8 m $Mg(TFSI)_2$-85%PEG-15%H_2O exhibit a dominant peak at 0.20 nm, corresponding to the first solvation shell of Mg^{2+}. After adding PEG, an additional

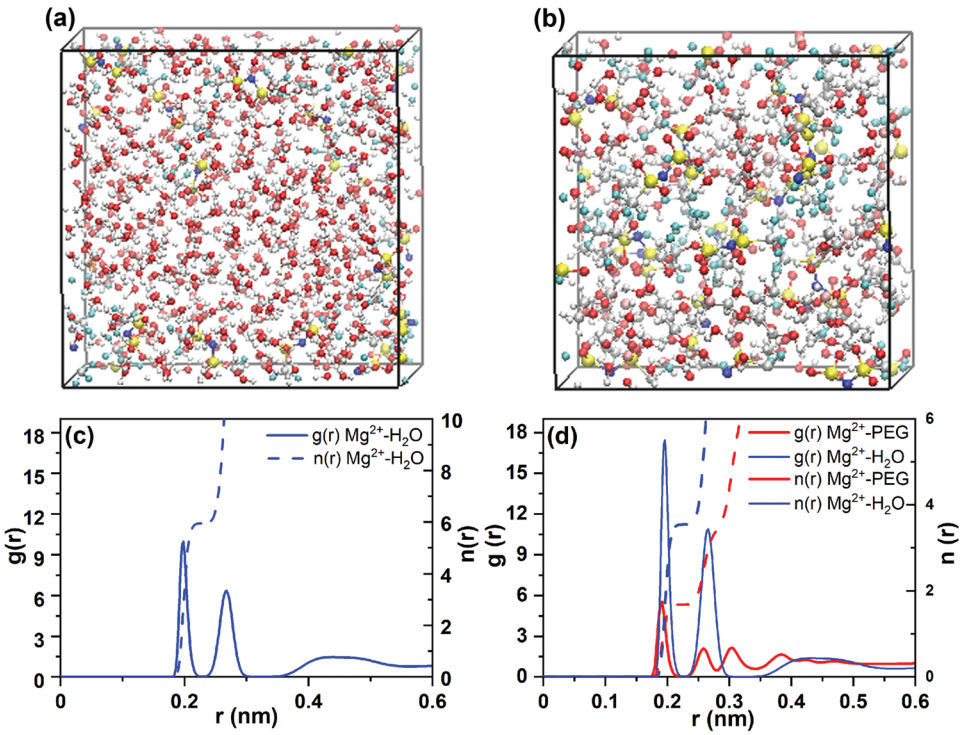

Figure 3. Density functional theory (DFT) and molecular dynamics (MD) of electrolytes. The simulated geometrical structure of a) 0.8 m $Mg(TFSI)_2$-H_2O and b) 0.8 m $Mg(TFSI)_2$-85%PEG-15%H_2O. Hydrogen, carbon, oxygen, fluorine, magnesium, sulfur, and nitrogen atoms are marked with white, gray, red, cyan, pink, yellow, and blue, respectively. The radial distribution function (RDF) g(r) and corresponding integrated coordination numbers (ICN) n(r) of Mg^{2+}-H_2O/PEG in both c) 0.8 m $Mg(TFSI)_2$-H_2O and d) 0.8 m $Mg(TFSI)_2$-85%PEG-15%H_2O.

peak appears at 0.19 nm, corresponding to Mg^{2+}-PEG with an ICN = 2, and the ICN of Mg^{2+}-H_2O sharply decreases from 5.47 to 3.5. This implies that 36% of the water in the first solvation shell is replaced by two PEG molecules, confirming the significant changes of Mg^{2+} solvation structure. Conversely, 0.73 $TFSI^-$ is coordinated with the first solvation shell of Mg^{2+} in 0.8 m $Mg(TFSI)_2$-85%PEG-15%H_2O (Figure S4e, Supporting Information), demonstrating the "'quasi-water-in-salt"' property of this electrolyte due to the direct coordination of Mg^{2+} and $TFSI^-$. The results identify that all water molecules in 0.8 m $Mg(TFSI)_2$-100%H_2O are connected while dissociated Mg^{2+} cations and $TFSI^-$ anions are fully solvated with water. The addition of PEG breaks the water networking and allows direct contacts between Mg^{2+} and $TFSI^-$, while part of water molecules are replaced and PEG and $TFSI^-$ do form a new network through the bonding with H_2O and Mg^{2+}.

2.2. Electrochemical Properties of V_2O_5 Nanowires Using the High Voltage AME

To demonstrate the applicability of $Mg(TFSI)_2$-85%PEG-15%H_2O electrolyte, V_2O_5 nanowires synthesized via hydrothermal method were selected as a cathode material for AMIBs. X-ray powder diffraction (XRD) demonstrates the V_2O_5 nanowires crystalize in an orthorhombic structure with space group $Pmn2_1$ and an interplanar spacing of 4.4 Å (Figure S5a, Supporting Information) Rietveld refinement exhibits the lattice parameters are a = 11.514 Å, b = 4.375 Å, and c = 3.567 Å. Scanning electron microscopy (SEM) demonstrates that V_2O_5 has an average length of more than 10 µm and a width of ≈30 nm (Figure S5b, Supporting Information). **Figure 4**a shows cyclic voltammograms (CVs) of V_2O_5 at 0.05 mV s^{-1} where V_2O_5 exhibits two very broad reduction peaks at 2.25 and 1.76 V and one oxidation peak at 3.0 V for the first scan. In the following two scans, both reduction and oxidation peaks show notable changes with the strong decrease with their intensities, indicating the large irreversible capacity. In contrast, CV displays significant differences in the 0.8 m $Mg(TFSI)_2$-100%H_2O electrolyte (Figure S6, Supporting Information), where it shows two broad reduction peaks at 1.92 and 2.44 V (with a shoulder at 2.50 V) and two oxidation peaks at 2.49 and 2.80 V for the first scan. In the following two scans, those peaks show strong decrease in intensity and one pair of redox peaks appear at 2.28/2.32 V. With the scan rate increase, the overall CVs of V_2O_5 nanowires in $Mg(TFSI)_2$-85%PEG-15%H_2O do not change much (Figure 4b), but the redox peaks become wider and move toward lower/higher potentials for reduction/oxidation. Generally, peak current (i) and scan rate (v) obey the power-law relationship[13] of $i = av^b$. According to the linear fitting of log(i) versus log(v), the oxidation/reduction of V_2O_5 exhibits b values of 0.56/0.62 (Figure 4c), indicating a diffusion-controlled process.

Charge-discharge cycling of the V_2O_5 nanowires was performed in the potential window of 1.58–3.68 V versus Mg^{2+}/Mg. The electrode displays two clear plateaus (at 2.41 and 1.93 V, respectively) on the first discharge profile and one slope-like plateau at around 2.74 V on the first charge profile (**Figure 5**a).

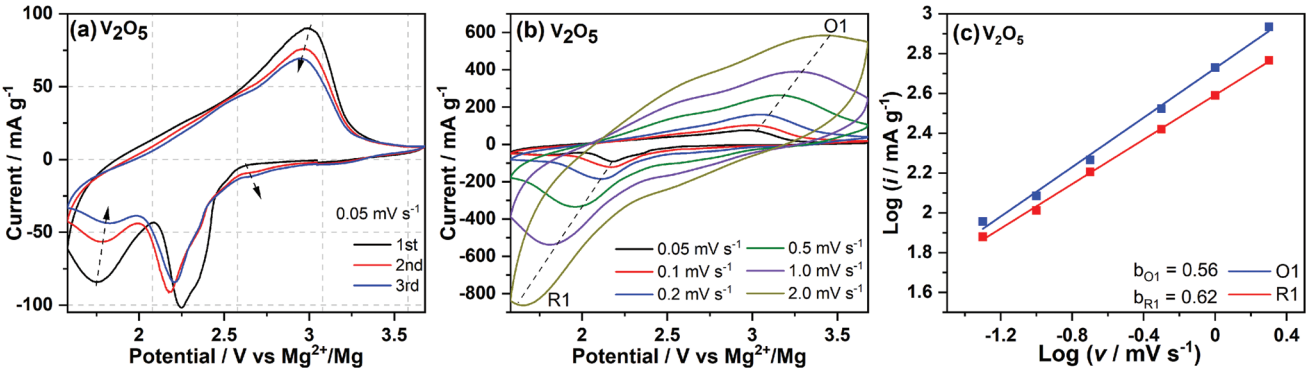

Figure 4. a) Cyclic voltammetry (CV) at a scan rate of 0.05 mV s^{-1} in the potential range of 1.58–3.68 V versus Mg^{2+}/Mg, where the arrows indicate the tendency of changes from the first to the third cycle, b) CV curves at different sweeping rates and their c) log(*i*) versus log(*ν*) plots and linear fittings of V_2O_5. All electrochemical properties were studied using three-electrode cells using V_2O_5 nanowires working electrode, activated carbon counter electrode, and AgCl/Ag reference electrode.

During subsequent cycling, the plateau at 2.41 V in charge becomes shorter and the plateau at 1.93 V in discharge gradually transforms into a sloped profile. Meanwhile, the slope-like charge plateau gradually becomes shorter with a slight increase of slope-plateau. The electrode shows a first discharge/charge capacity of 359/326 mAh g^{-1}, resulting in ≈91% initial coulombic efficiency (Figure 5a). Afterward, the discharge capacity decreases to 286 mAh g^{-1} after 100 cycles, yielding 80% capacity retention (Figure 5b), which exhibits superior performance compared with that in 0.8 m $Mg(TFSI)_2$-100%H_2O (Figure S7, Supporting Information). Rate capability test (Figure 5d) demonstrates that the V_2O_5 nanowires can deliver an average discharge capacity of 242, 178, 147, 101, and 54 mAh g^{-1} at current densities of 50, 100, 200, 500, and 1000 mA g^{-1}, respectively. When the current returns to 50 mA g^{-1}, V_2O_5 delivers a specific capacity of ≈225 mAh g^{-1}, followed by a slow increase of capacity to ≈250 mAh g^{-1} at the 40th cycle and then a gradual capacity fading to ≈214 mAh g^{-1} at 60th cycle. The electrode exhibits larger and larger electrode polarization along with the increase of current densities (Figure 5c), suggesting the kinetics properties of V_2O_5 nanowires at high current densities strongly depend on electrolyte's properties, particularly ionic conductivity. Compared with recent literature (Table S6, Supporting Information), our AMIB cell using V_2O_5 cathode material exhibited much improved electrochemical performance in terms of discharge capacity and cycling stability. As a result, the high voltage aqueous electrolyte reported in this work makes it possible to develop high-performance AMIBs with better cycle stability.

2.3. Reaction Mechanism of Vanadium Oxide Cathodes in AMIBs

Ex situ XRD was performed on V_2O_5 at different discharge/charge states to study their structure evolution during Mg^{2+} intercalation/deintercalation (**Figure 6**a). Some new reflections appear at 2.41 V (about 25% of depth of discharge).

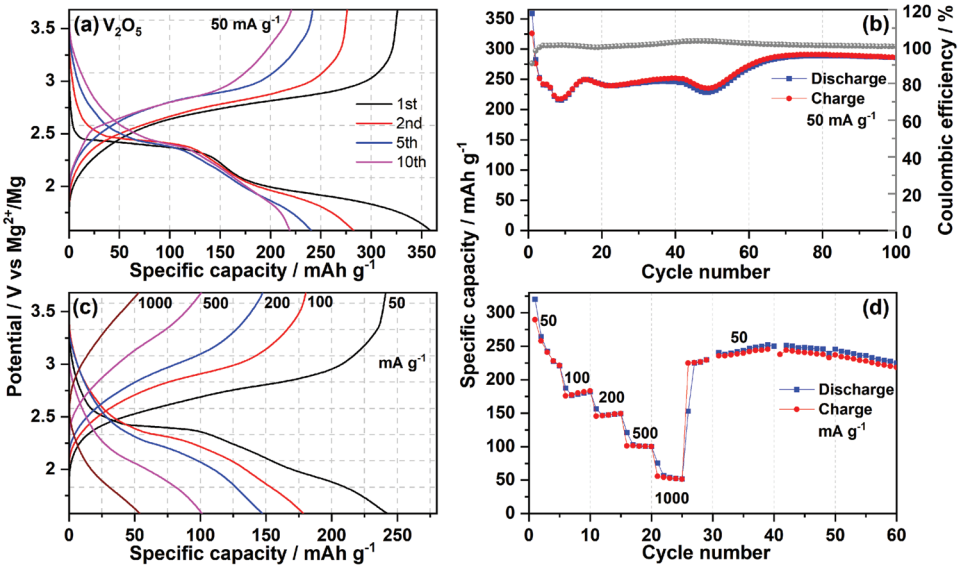

Figure 5. a) Charge–discharge curves and b) cycling performance of V_2O_5 at 50 mA g^{-1}; c) Charge–discharge curves at different specific currents, and d) rate performance in 0.8 m $Mg(TFSI)_2$-85%PEG-15%H_2O in the potential range of 1.58–3.68 V versus Mg^{2+}/Mg.

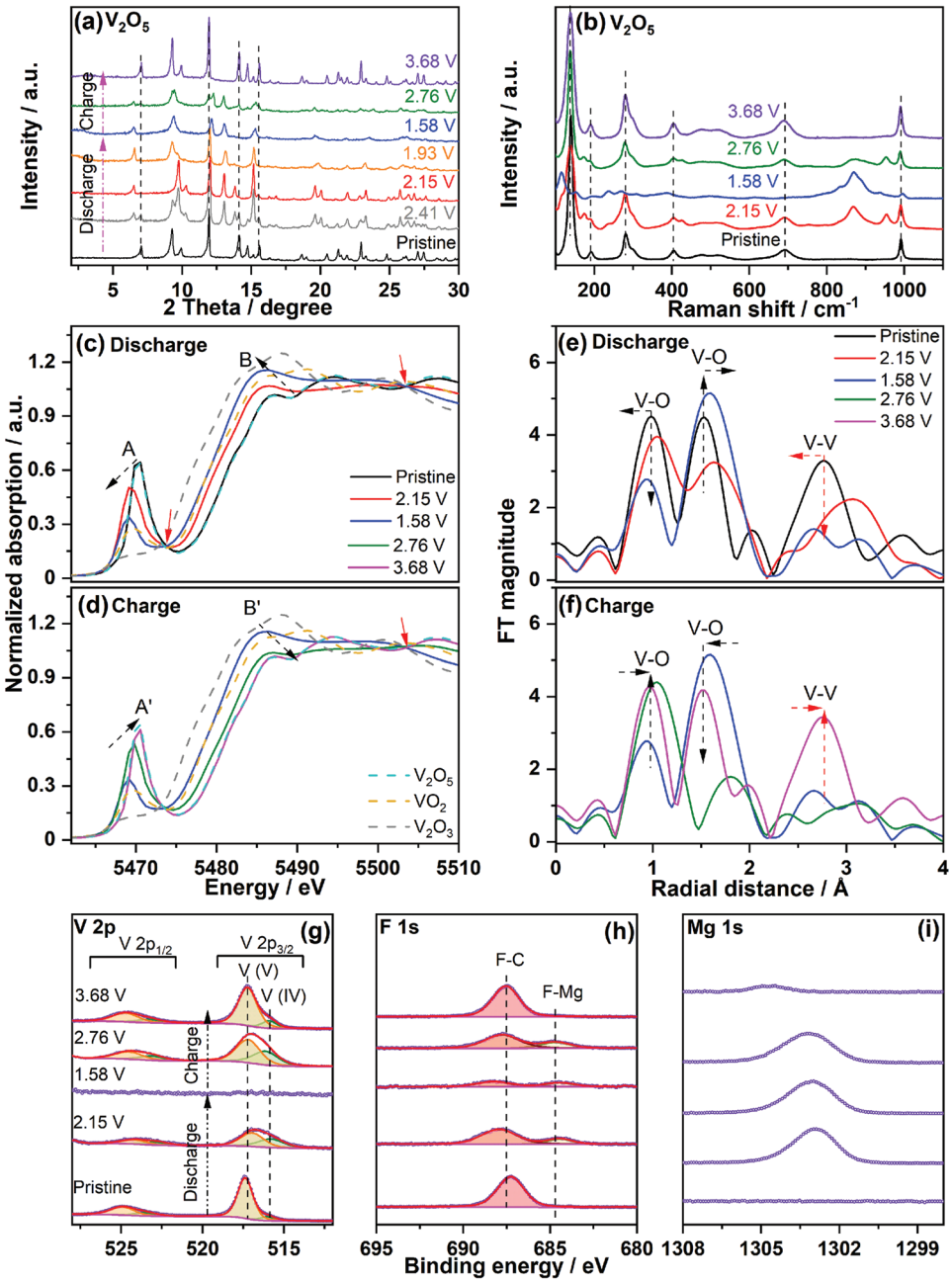

Figure 6. a) Ex situ XRD, b) Raman spectra, c,d) X-ray absorption spectroscopy (XAS) for the V K-edge, e,f) phase-uncorrected Fourier transforms (FT) of V K-edge EXAFS (k^3-weighted), and g,h,i) V 2p, F 1s and Mg 1s X-ray photoelectron spectra of V_2O_5 at different discharge/charge states (Mo $K_{\alpha 1}$ radiation, $\lambda = 0.70932$ Å); the isosbestic points in (c,d) are indicated by red arrows.

Upon discharge to 2.15 V (about 50% of depth of discharge), all reflections of V_2O_5 disappear and the obtained reflections of the formed Mg-rich $Mg_xV_2O_5$ ($x \approx 0.6$) (see Rietveld refinement Figure S8a (Supporting Information), space group $Pmn2_1$, lattice parameters $a = 12.503$ Å, $b = 4.180$ Å, and $c = 3.526$ Å) are in good match with ε-$Mg_{0.6}V_2O_5$ from our previous work,[2i] indicating a 2-phase transition process. With further Mg^{2+} intercalation to 1.93 and 1.58 V (about 75% and 100% of depth of discharge), the disappearance of new reflections from $Mg_xV_2O_5$ ($x \approx 0.6$) suggests a second 2-phase transition process to form Mg-rich $Mg_xV_2O_5$ ($x \approx 1.0$) phase (Figure S8b, Supporting Information). This is the first report of this $Mg_xV_2O_5$ ($x \approx 1.0$) phase formed at room temperature via electrochemical Mg-ion intercalation and detected via XRD. Upon charging to 2.76 V (50% of depth of charge), the reflections of V_2O_5 re-appear and co-exist with Mg-rich $Mg_xV_2O_5$ ($x \approx 1.0$) phase (Figure S8c, Supporting Information) and finally, all reflections at 3.68 V (100% of depth of charge) recover to their initial positions with lower intensities, implying a reversible 2-phase transition but asymmetry during cycling.

To investigate the local structure of the materials during Mg^{2+} (de)intercalation, Raman scattering was performed on the pristine and cycled samples. V_2O_5 nanowires display typical Raman peaks (Figure 6b) as reported in previous work.[14] Significant structural changes are detected for V_2O_5 after Mg^{2+} intercalation (Figure 6b). Upon Mg^{2+} intercalation to 2.15 V, the peak at 140 cm^{-1} shifts to 138 cm^{-1} with the decrease of the intensity, meanwhile, some new peaks appear at 174, 427, 753, 869, and 954 cm^{-1}. With further Mg^{2+} intercalation to 1.58 V, only some small and broad peaks (115, 153, 237, 268, 389, 834, 871, 939, and 997 cm^{-1}) are observed due to local structure in the $Mg_xV_2O_5$ ($x \approx 1.0$) phase. Upon charging (2.76 and 3.68 V), the Raman spectra show reversible changes and finally return to its original state of V_2O_5, indicating the high reversibility.

The electronic and structural environments of V-ions at various charged/discharged states are studied by X-ray absorption spectroscopy (XAS). The edge position of the initial state V_2O_5 is slightly lower than that of the V_2O_5 reference. Herein, the oxidation state of V is confirmed to be mainly +5, in agreement with the XPS result for pristine V_2O_5. Upon Mg^{2+} intercalation into V_2O_5, the edge energy of V K-edge and pre-edge peak shift toward lower values, implying reduction of V ions to V^{4+} (Figure 6c). The intensity decrease of the pre-edge peak indicates an increase in the symmetry of V ions due to the decreased probability of the 1s and bound p hybridized d-state transitions.[15] Meanwhile, two broad peaks of edge resonance (B) emerge to a single broad peak with the increase of intensity, which is ascribed to energy absorption by core electrons.[15b] Moreover, distinct isosbestic points are detected for both discharge at ≈5474 and ≈5503 eV and charge at ≈5504 eV processes, indicating a 2-phase reaction.[16] The edge position of the electrode at 1.58 V (100% of depth of discharge) overlaps with that of VO_2 reference, indicating the oxidation state of V is confirmed to be +4. Upon Mg^{2+} deintercalation, the edge energy of V K-edge, pre-edge peak, and edge resonance display reversible behavior, indicating the oxidation of V ions and reversibility of local structure (Figure 6d). The local structure changes of V ions were further studied by analyzing the phase-uncorrected Fourier transform (FT) (k^3-weighted) of the V K-edge extended X-ray absorption fine structure (EXAFS). The pristine V_2O_5 shows two FT peaks at 1.0 and 1.53 Å, corresponding to the V–O bonds in VO_6 octahedra, and one FT peak at 2.76 Å assigned to the V–V shell.[17] During discharge, the V–O features shift to lower and higher radial distances with strongly decreased (peak at 1.0 Å) and slightly increased amplitudes (peak at 1.53 Å) (Figure 6e), indicating the overall symmetry increase of the local structure around V. Meanwhile, the V–V feature decreases its amplitude with shifts to lower value. These results indicate that the intercalated Mg^{2+} affect both V–O and V–V shell structure. During charging, they show reversible behavior and almost return to their initial positions (Figure 6f), demonstrating the high reversibility of V_2O_5.

The surface chemistry and elemental composition of the pristine and cycled cathodes are studied by X-ray photoelectron spectroscopy (XPS). The V 2p spectrum of pristine V_2O_5 can be fitted by two doublets with V $2p_{3/2}$ at 517.2 and 515.9 eV,[18] respectively, resulting in an average oxidation state of $V^{4.92+}$ (Figure 6g–i). The V ions are gradually reduced to $V^{4.60+}$ when discharged to 2.15 V. Meanwhile, the V $2p_{3/2}$ peak gradually decreases in intensity and totally disappears at the end of discharge, indicating that the surface of the V_2O_5 cathode is covered by a newly formed cathode electrolyte interphase (CEI) film. The F 1s spectrum of pristine V_2O_5 shows one peak at 687.3 eV related to C–F bond, which is attributed to the PVDF binder.

Upon discharge, two new peaks at 684.7 (refers to F–Mg bond) and 1303 eV (refers to Mg–F bond) are observed for F 1s and Mg 1s. These new XPS signals confirm that the main component of the CEI film is MgF_2, which could be attributed to the decomposition of $TFSI^-$. Upon charge to 2.76 and 3.68 V, V $2p_{3/2}$ peak reappears and increases in intensity with oxidation state of $V^{4.60+}$ and $V^{4.86+}$, respectively. Surprisingly, it is noticed that along with the decrease/increase of the V $2p_{3/2}$ peak, the F 1s peak increases/decreases accordingly. This indicates reversible formation/decomposition of the CEI film during discharge-charge cycling. Overall, the V_2O_5 cathode returns to its pristine state accompanied by reversible CEI formation and decomposition during cycling.

3. Conclusion

A series of AMEs show a stable ESW of ≈3.7 V using a low-salt concentration of 0.8 m $Mg(TFSI)_2$. The electrochemical/physicochemical properties of AME and water splitting suppression are strongly affected by the addition of PEG 400 molecular crowding agent. V_2O_5 nanowires show a discharge capacity of 286 mAh g^{-1} after 100 cycles with capacity retention of 80% at 50 mA g^{-1} in the 0.8 m $Mg(TFSI)_2$-85%PEG-15%H_2O AME. A Mg-rich $Mg_xV_2O_5$ ($x \approx 1.0$) phase is for the first time observed via XRD through electrochemical Mg-ion intercalation at room temperature. Meanwhile, a reversible formation/decomposition of CEI in AMIBs is revealed for the first time, where MgF_2 originating from the decomposition of $TFSI^-$ is identified as the dominant component. Not only electrolyte but also the crystal structure can affect the electrochemical performance, particularly at high current densities. This work paves the way to novel multivalent aqueous batteries by using a low-salt concentration AME and provides an approach for designing high-performance cathode materials and eco-friendly, high-voltage, high-safety, and low-cost aqueous electrolytes for sustainable large-scale energy storage.

4. Experimental Section

Synthesis of V_2O_5 Nanowires: V_2O_5 nanowires were prepared via a hydrothermal method. Briefly, 0.5 g of commercial V_2O_5 powder (Alfa Aesar, 99.99%) was added to 25 mL of deionized water under vigorous stirring for 10 min to form a light orange suspension. Then, 5 mL 30% hydrogen peroxide (H_2O_2) was dropwise added to the above suspension with stirring for 20 min to get a transparent reddish-brown solution. The obtained solution was transferred to a 45 mL Teflon-lined stainless-steel autoclave and kept at 220 °C for 48 h. The precipitate was washed with deionized H_2O and ethanol several times and dried at 75 °C for 12 h.

Preparation and Characterizations of the Electrolyte: $Mg(TFSI)_2$ was dissolved into a series of polyethylene glycol 400 (PEG 400) and pure H_2O solvent with vigorous stirring overnight at room temperature to form 0.8 m $Mg(TFSI)_2$-xPEG-(1-x)H_2O (x = 0%, 75%, 80%, 85%, 90%, and 95%). Ionic conductivity was measured by using Mettler Toledo InLab 738 ISM at 25 °C.

Fourier-transform infrared spectroscopy (FTIR) was performed on a Bruker Alpha-P instrument with attenuated total reflection (ATR) technology in the frequency range of 4000–400 cm^{-1}. The viscosity of various electrolytes was measured on a Bohlin Gemini 200 Nano rheometer at 25 °C with 40/1° cone geometry by using a solvent evaporation protection cover. Measurements were conducted with the shear rate varied from 1 to 200 s^{-1} (viscosity is generally independent of shear rate). ^1H nuclear magnetic resonance (NMR) spectroscopy was performed on the electrolyte samples with a Bruker Avance 300 MHz spectrometer at a magnetic field of 7.0 T. Samples were placed inside 5 mm glass tubes and chemical shifts are given relative to that of tetramethylsilane at 0 ppm.

Morphological and Structural Study: The morphologies were studied with a Zeiss Supra 55 Scanning Electron Microscope (SEM) with primary energy of 15 keV. The structural characterizations were performed on a STOE STADI P diffractometer operated with Mo $K_{\alpha 1}$ radiation (λ = 0.70932 Å). The powders were filled in 0.5 mm Ø boro-silicate capillaries, and diffraction patterns were collected in capillary geometry. A LabRam HR Evolution Raman microscope from Horiba Scientific equipped with HeNe laser (633 nm, 17 mW) and a CCD detector (Horiba) was used to collect the Raman scattering of the samples. Meanwhile, a 600 gr/mm grating was used to split the measurement signal with a ×100 objective (NA 0.95) for all the pristine and cycled samples. The washed and dried electrodes after discharge and charge were sealed in an in situ cell with a quartz window inside a glovebox, where the quartz window is suitable for ex situ Raman measurements. X-ray photoelectron spectroscopy (XPS) was performed using a K-Alpha spectrometer (ThermoFisher Scientific, UK) equipped with a microfocused, monochromated Al K_α X-ray source (λ = 1486.6 eV) with a spot size of 400 µm. A charge compensation system was employed during the measurement, using electrons of 8 eV energy and low-energy argon ions to prevent localized charge accumulation. All samples were prepared in an argon-filled glove box and transferred under an inert atmosphere into the spectrometer. Thermo Avantage software was used in data acquisition and processing, as described elsewhere.[19] The analyzer transmission function, Scofield sensitivity factors, and effective attenuation lengths for photoelectrons were applied for quantification.[20] The standard TPP-2M formalism was used for the calculation of effective attenuation lengths.[21] All spectra were referenced to the carbonaceous C 1s peak (C–C/C–H) at 285.0 eV binding energy.

Electrochemical Characterizations: The electrode was prepared by coating slurry mixture on stainless steel foil, which consists of active material V_2O_5 with C65 (Timcal) and polyvinylidene difluoride (PVDF) binder in a weight ratio of 70:20:10 with N-Methyl-2-pyrrolidone solvent. The electrode was dried at 65 °C overnight and then cut into discs of 12 mm diameter (mass loading of ≈1.3 mg cm^{-2}). Activated carbon (AC) electrode was prepared using AC, C65 (Timcal) and polytetrafluoroethylene (PTFE, 60 wt% solution in water from Sigma–Aldrich) in a weight ratio of 8:1:1 with solvent isopropanol in a DAC150.1 FVZ model from SpeedMixer with 800 rpm for 10 min. The paste mixture was kneaded manually on a glass plate and finally was rolled to a uniform thickness electrode. The electrodes were finally dried at 70 °C overnight under vacuum before use. The LSVs of various electrolytes were performed using a glass cell consisting of glassy carbon (GC) (and stainless steel foil) working electrode, Pt plate counter electrode, and AgCl/Ag reference electrode. Three-electrode Swagelok-type cells for electrochemical measurements were assembled in air at room temperature. The cells were built with V_2O_5 positive electrode, AC counter electrode, AgCl/Ag reference electrode (3 M NaCl), 0.8 m $Mg(TFSI)_2$-85%PEG-15%H_2O or 0.8m $Mg(TFSI)_2$-100%H_2O as an electrolyte (700 µL), and a piece of glass microfiber (Whatman) as the separator. The mass of AC was intentionally in excess with a large N/P ratio of about 9–12. AC was used as the counter electrode due to its high surface area, which can provide sufficient charge storage via electrical double-layer capacitance to guarantee full charge balance during Mg intercalation.[2h,22] Note that the specific capacities in this work were calculated according to the weight of the V_2O_5 active cathode material. Galvanostatic cycling with potential limitation (GCPL) and cyclic voltammetry (CV) measurements were performed in the potential range of [–1.0, 1.1 V] and [–0.75, 0.75 V] (vs AgCl/Ag, 3 M NaCl) in 0.8 m $Mg(TFSI)_2$-85%PEG-15%H_2O and 0.8m $Mg(TFSI)_2$-100%H_2O on a VMP3 potentiostat (BioLogic) at 25 °C, corresponding to [1.58, 3.68 V] and [1.88–3.33 V] versus Mg^{2+}/Mg, respectively. GCPL was performed at different current densities ranging from 50 to 1000 mA g^{-1} to determine the rate capability of the electrodes. All potentials have been converted to Mg^{2+}/Mg reference for convenience based on the voltage difference of 2.58 V between AgCl/Ag and Mg^{2+}/Mg.

Sample Preparation for Ex Situ Characterizations: The V_2O_5 cells at 25% (2.41 V), 50% (2.15 V), 75% (1.93 V), 100% (1.58 V) depth of discharge and 50% (2.76 V), 100% (3.68 V) depth of charge were disassembled and then the cathode was washed with acetonitrile in an Ar-filled glovebox. After dried in a vacuum chamber, the electrode composite was peeled off and filled into 0.5 mm Ø boro-silicate capillaries for ex situ XRD measurements. Note that the reference electrode was removed before putting the cells into glovebox.

Ex situ X-ray absorption spectroscopy (XAS) measurements were carried out at PETRA-III beamline P65 at DESY in Hamburg. XAS spectra were recorded in quick-XAS (6 min/spectrum) mode in fluorescence geometry using a PIPS diode. The V K-edge of V_2O_5 at different states (sealed in two pieces of Kapton foils) was measured and the energy was calibrated using the absorption edge of V foil, as it is commonly employed in XAS experiments. V_2O_5, VO_2, and V_2O_3 were used as standard materials. All data were collected at room temperature with a Si (111) double crystal monochromator and all XAS spectra were processed using DEMETER software package.[23]

Molecular Dynamics Simulations: All atomistic molecular dynamics (MD) simulations were performed with the GROMACS 4.6.7 package.[24] The GROMOS force field[25] was used for all components. The MD simulations were carried out using cubic cells with a linear dimension of 2.83 nm for 0.8 m $Mg(TFSI)_2$-H_2O (containing 9 $Mg(TFSI)_2$ and 600 H_2O) and 2.18 nm for 0.8 m $Mg(TFSI)_2$-85%PEG-15%H_2O (containing 10 $Mg(TFSI)_2$, 100 H_2O, and 25 PEG) using the software package PACKMOL.[26] In all simulations, the temperature was kept constant at T = 300 K by an improved velocity-rescaling thermostat,[27] using a coupling time constant of 0.1 ps. The pressure was kept constant at p = 1 bar by a semi-isotropic Parrinello-Rahman barostat[28] with coupling time constant of 2 ps and compressibility 4.5× 10^5 bar 1. Electrostatic interactions were treated through the Particle Mesh Ewald method[29] with a real-space cut-off of 1.0 nm and a grid spacing of 0.16 nm with fourth-order interpolation scheme. Lennard-Jones interactions were truncated at 1.0 nm and shifted to zero. A Leapfrog algorithm with an elementary time step of 2 fs was used for numerical integration. All bonds were constrained by the LINCS algorithm.[30] Prior to production runs, an energy minimization was first performed using a conjugate-gradient method, followed by an equilibration of the system for 10 ns under constant volume constant temperature conditions, and a subsequent equilibration run of 10 ns under constant temperature and constant pressure conditions. These final production runs at constant temperature and pressure had a length of more than 150 ns each.

Supporting Information

Supporting Information is available from the Wiley Online Library or from the author.

Acknowledgements

This work contributes to the research performed at CELEST (Center for Electrochemical Energy Storage Ulm-Karlsruhe) and was partially funded by the Deutsche Forschungsgemeinschaft (DFG, German Research Foundation) under Germany´s Excellence Strategy – EXC 2154 – Project ID 390874152 (POLiS Cluster of Excellence). This work was also supported by National Natural Science Foundation of China (No. 51972140). The K-Alpha instrument was financially supported by the Federal Ministry of Economics and Energy (BMWi) on the basis of a decision by the German Bundestag. The authors acknowledge the synchrotron radiation source

Petra-III (DESY) in Hamburg, Germany, for the provision of beamtime at the P65 beamline. The authors would like to thank Dr. Edmund Welter and Dr. Morgane Desmau from Experiments Division at DESY, Hamburg, for technical support. The authors also want to acknowledge the support and collaboration from Dr. Andreas Hofmann and Prof. Thomas Hanemann within POLiS. The authors thank Dr. Kristina Pfeifer (IAM-ESS) for her contribution to SEM measurements. The authors greatly appreciate Mrs. Liuda Mereacre for her support in Raman measurements.

Open access funding enabled and organized by Projekt DEAL.

Conflict of Interest

The authors declare no conflict of interest.

Author Contributions

Q.F. conceived the idea and discussed with X.W., X.L., S.I., A.S., M.B., Z.W., M.K., H.E., Y.W., and S.D.; Q.F. performed material synthesis, electrolyte/sample preparation, characterizations, electrochemical measurements, and analyzed the data. Z.W. carried out viscosity measurements and analyzed viscosity data. M.B. performed FTIR and analyzed the data. S.I. conducted NMR and analyzed the data. X.L. performed XPS and Raman measurements and analyzed the XPS data and Q.F. analyzed the Raman data. A.S. and Q.F. carried out XAS and analyzed the data. X.W. carried out DFT and MD calculations and analyzed the data with Y.W. Q.F. wrote the preliminary draft with input from X.W. and Y.W.; Q.F., M.K., H.E., S.D., and Y.W. discussed the results and revised the manuscript. All authors contributed to interpreting the findings, reviewing, and commenting on the manuscript.

Data Availability Statement

The data that support the findings of this study are available from the corresponding author upon reasonable request.

Keywords

aqueous Mg-ion batteries, aqueous Mg-ion electrolytes, molecular dynamics simulations, nuclear magnetic resonance, vanadium oxide, X-ray absorption spectroscopy

Received: October 21, 2021
Revised: December 9, 2021
Published online:

[1] a) M. Mao, T. Gao, S. Hou, C. Wang, *Chem. Soc. Rev.* **2018**, *47*, 8804; b) F. Wang, X. Fan, T. Gao, W. Sun, Z. Ma, C. Yang, F. Han, K. Xu, C. Wang, *ACS Cent. Sci.* **2017**, *3*, 1121.

[2] a) E. Sheha, E. M. Kamar, *Mater. Sci. Poland* **2019**, *37*, 570; b) C. L. Zuo, Y. Xiao, X. J. Pan, F. Y. Xiong, W. W. Zhang, J. C. Long, S. J. Dong, Q. Y. An, P. Luo, *ChemSusChem* **2021**, *14*, 2093; c) R. Attias, M. Salama, B. Hirsch, R. Pant, Y. Gofer, D. Aurbach, *ACS Energy Lett.* **2019**, *4*, 209; d) X. Du, G. Huang, Y. Qin, L. Wang, *RSC Adv.* **2015**, *5*, 76352; e) I. D. Johnson, G. Nolis, L. Yin, H. D. Yoo, P. Parajuli, A. Mukherjee, J. L. Andrews, M. Lopez, R. F. Klie, S. Banerjee, B. J. Ingram, S. Lapidus, J. Cabana, J. A. Darr, *Nanoscale* **2020**, *12*, 22150; f) D. Kim, J. H. Ryu, *Electron. Mater. Lett.* **2019**, *15*, 415; g) A. Mukherjee, S. Taragin, H. Aviv, I. Perelshtein, M. Noked, *Adv. Funct. Mater.* **2020**, 30, 2003518; h) J. L. Andrews, A. Mukherjee, H. D. Yoo, A. Parija, P. M. Marley, S. Fakra, D. Prendergast, J. Cabana, R. F. Klie, S. Banerjee, *Chem* **2018**, *4*, 564; i) Y. Cheng, Y. Shao, V. Raju, X. Ji, B. L. Mehdi, K. S. Han, M. H. Engelhard, G. Li, N. D. Browning, K. T. Mueller, J. Liu, *Adv. Funct. Mater.* **2016**, *26*, 3446; j) Q. Fu, A. Sarapulova, V. Trouillet, L. Zhu, F. Fauth, S. Mangold, E. Welter, S. Indris, M. Knapp, S. Dsoke, N. Bramnik, H. Ehrenberg, *J. Am. Chem. Soc.* **2019**, *141*, 2305; k) G. Gershinsky, H. D. Yoo, Y. Gofer, D. Aurbach, *Langmuir* **2013**, *29*, 10964; l) H. D. Yoo, J. R. Jokisaari, Y.-S. Yu, B. J. Kwon, L. Hu, S. Kim, S.-D. Han, M. Lopez, S. H. Lapidus, G. M. Nolis, B. J. Ingram, I. Bolotin, S. Ahmed, R. F. Klie, J. T. Vaughey, T. T. Fister, J. Cabana, *ACS Energy Lett.* **2019**, *4*, 1528.

[3] a) L. Chen, J. L. Bao, X. Dong, D. G. Truhlar, Y. Wang, C. Wang, Y. Xia, *ACS Energy Lett.* **2017**, *2*, 1115; b) D. Chao, W. Zhou, F. Xie, C. Ye, H. Li, M. Jaroniec, S.-Z. Qiao, *Sci. Adv.* **2020**, *6*, eaba4098.

[4] a) L. Suo, O. Borodin, T. Gao, M. Olguin, J. Ho, X. Fan, C. Luo, C. Wang, K. Xu, *Science* **2015**, *350*, 938; b) L. Suo, O. Borodin, W. Sun, X. Fan, C. Yang, F. Wang, T. Gao, Z. Ma, M. Schroeder, A. von Cresce, S. M. Russell, M. Armand, A. Angell, K. Xu, C. Wang, *Angew. Chem.* **2016**, *55*, 7136; c) Y. Yamada, K. Usui, K. Sodeyama, S. Ko, Y. Tateyama, A. Yamada, *Nat. Energy* **2016**, *1*, 16129; d) S. Ko, Y. Yamada, K. Miyazaki, T. Shimada, E. Watanabe, Y. Tateyama, T. Kamiya, T. Honda, J. Akikusa, A. Yamada, *Electrochem. Commun.* **2019**, *104*, 106488.

[5] D. Chao, S.-Z. Qiao, *Joule* **2020**, *4*, 1846.

[6] D. Kilburn, J. H. Roh, L. Guo, R. M. Briber, S. A. Woodson, *J. Am. Chem. Soc.* **2010**, *132*, 8690.

[7] L. A. Ferreira, V. N. Uversky, B. Y. Zaslavsky, *Mol. BioSyst.* **2017**, *13*, 2551.

[8] J. Xie, Z. Liang, Y.-C. Lu, *Nat. Mater.* **2020**, *19*, 1006.

[9] C. Schreiner, S. Zugmann, R. Hartl, H. J. Gores, *J. Chem. Eng. Data* **2010**, *55*, 1784.

[10] M. Z. Jora, M. V. C. Cardoso, E. Sabadini, *J. Mol. Liq.* **2016**, *222*, 94.

[11] N. Dubouis, P. Lemaire, B. Mirvaux, E. Salager, M. Deschamps, A. Grimaud, *Energy Environ. Sci.* **2018**, *11*, 3491.

[12] J. E. Huheey, *J. Org. Chem.* **1971**, *36*, 204.

[13] G. A. Muller, J. B. Cook, H.-S. Kim, S. H. Tolbert, B. Dunn, *Nano Lett.* **2015**, *15*, 1911.

[14] R. Baddour-Hadjean, J. P. Pereira-Ramos, C. Navone, M. Smirnov, *Chem. Mater.* **2008**, *20*, 1916.

[15] a) T. Tanaka, H. Yamashita, R. Tsuchitani, T. Funabiki, S. Yoshida, *J. Chem. Soc., Faraday Trans. 1* **1988**, *84*, 2987; b) J. Wong, F. W. Lytle, R. P. Messmer, D. H. Maylotte, *Phys. Rev. B* **1984**, *30*, 5596.

[16] X. Liu, D. Wang, G. Liu, V. Srinivasan, Z. Liu, Z. Hussain, W. Yang, *Nat. Commun.* **2013**, *4*, 2568.

[17] a) S. Stizza, G. Mancini, M. Benfatto, C. R. Natoli, J. Garcia, A. Bianconi, *Phys. Rev. B: Condens. Matter Mater. Phys.* **1989**, *40*, 12229; b) A. N. Mansour, P. H. Smith, M. Balasubramanian, J. McBreen, *J. Electrochem. Soc.* **2005**, *152*, A1312; c) M. Giorgetti, *J. Electrochem. Soc.* **1999**, *146*, 2387.

[18] G. Silversmit, D. Depla, H. Poelman, G. B. Marin, R. De Gryse, *J. Electron Spectrosc. Relat. Phenom.* **2004**, *135*, 167.

[19] K. L. Parry, A. G. Shard, R. D. Short, R. G. White, J. D. Whittle, A. Wright, *Surf. Interface Anal.* **2006**, *38*, 1497.

[20] J. H. Scofield, *J. Electron Spectrosc. Relat. Phenom.* **1976**, *8*, 129.

[21] Tanuma, S. , C. J. Powell, D. R. Penn, *Surf. Interface Anal.* **2011**, *43*, 689.

[22] Y. Xu, X. Deng, Q. Li, G. Zhang, F. Xiong, S. Tan, Q. Wei, J. Lu, J. Li, Q. An, L. Mai, *Chem* **2019**, *5*, 1194.

[23] B. Ravel, M. Newville, *J. Synchrotron Radiat.* **2005**, *12*, 537.

[24] B. Hess, C. Kutzner, D. van der Spoel, E. Lindahl, *J. Chem. Theory Comput.* **2008**, *4*, 435.

[25] C. Oostenbrink, A. Villa, A. E. Mark, W. F. Van Gunsteren, *J. Comput. Chem.* **2004**, *25*, 1656.

[26] L. Martínez, R. Andrade, E. G. Birgin, J. M. Martínez, *J. Comput. Chem.* **2009**, *30*, 2157.

[27] G. Bussi, D. Donadio, M. Parrinello, *J. Chem. Phys.* **2007**, *126*, 014101.

[28] M. Parrinello, A. Rahman, *J. Appl. Phys.* **1981**, *52*, 7182.

[29] T. Darden, D. York, L. Pedersen, *J. Chem. Phys.* **1993**, *98*, 10089.

[30] B. Hess, H. Bekker, H. J. C. Berendsen, J. G. E. M. Fraaije, *J. Comput. Chem.* **1997**, *18*, 1463.